Optical Engineering

OpticalEngineering.SPIEDigitalLibrary.org

Reflection-mode digital gradient sensing method: measurement accuracy

Chengyun Miao
Hareesh V. Tippur

SPIE.

Chengyun Miao, Hareesh V. Tippur, "Reflection-mode digital gradient sensing method: measurement accuracy," *Opt. Eng.* **58**(4), 044101 (2019), doi: 10.1117/1.OE.58.4.044101.

Reflection-mode digital gradient sensing method: measurement accuracy

Chengyun Miao and Hareesh V. Tippur*
Auburn University, Department of Mechanical Engineering, Auburn, Alabama, United States

Abstract. Surface topography evaluation from measured surface slopes is critical in many engineering applications, including metrology of electronic substrates, optical elements, and small deformation measurement of engineering structures subjected to external thermomechanical stimuli. A recently proposed noncontact full-field optical method called reflection-mode digital gradient sensing (r-DGS) is able to measure small angular deflections of light rays proportional to two orthogonal surface slopes. It has been shown that submicron scale deformations can be detected by processing the slope data using a robust numerical integration scheme called the higher-order finite-difference-based least-squares integration. However, the smallest measurable deformations and the associated accuracy are yet to be determined. In our work, this very issue is addressed by carrying out experiments at temporally different recording frequencies, namely (a) ultrahigh-speed digital photography at 10^6 frames per second (fps) and (b) slow recording speeds of 10^1 fps. The results show that r-DGS is able to measure submicron out-of-plane deformations under latter conditions and nanoscale deformations in the former conditions. [DOI: 10.1117/1.OE.58.4.044101]

Keywords: optical metrology; speckle correlation; surface slopes; surface topography; noncontact evaluation.

Paper 190144 received Jan. 30, 2019; accepted for publication Mar. 11, 2019; published online Apr. 5, 2019.

1 Introduction

Accurate noncontact evaluation of surface topography is of great engineering significance. Optical methods based on interferometry and speckle correlation have been applied to such problems in the past. Recent research shows that it is more efficient for optical methods to measure surface slopes instead of measuring the absolute height values due to channel capacity limitations.[1] The surface slopes can then be converted to surface topography using integration algorithms. Thin substrates (silicon, glass, and quartz) are widely used in a number of areas—microelectronics to space structures. They are susceptible to a range of mechanical loading environments—dynamic impact to slow thermomechanical loading. Hence, accurate quantification of surface topography of thin structures under these conditions would be essential.

In the past, several optical methods with full-field and noncontact measurement capabilities have been proposed and applied to engineering problems. Chen et al.[2] reviewed different optical methods used to measure three-dimensional (3-D) shapes of objects. Moiré methods[3] and moiré interferometry[4,5] were applied by several researchers to study warpage and surface deformation of electronic components. Holographic interferometry is popular for vibration measurement.[6] Pedrini et al.[7] proposed a high-speed digital holographic interferometry to measure vibrations without temporal or spatial phase unwrapping. Hytch et al.[8] proposed a holographic moiré technique, a combination of the moiré technique and off-axis holography, to obtain nanometric fringe measurements in electronic devices. Shang et al.[9] reviewed several shearographic methods for surface profile measurement and indicated that shearography is a more practical tool when compared to holography since the former does not require vibration isolation. Tippur et al.[10,11] proposed a real-time lateral shearing interferometry, called the coherent gradient sensing, which can be applied to measure surface slopes of thin structures. Although interferometric methods are historically popular, the limitations in these methods are also obvious due to the requirements of coherent light source, sophisticated optical components, need for phase unwrapping from interference fringes, to name a few. In recent years, digital image correlation (DIC) methods have made way into this arena as they are capable of measuring both 2-D and 3-D deformations[12,13] without many of these restrictions. Some notable examples include works of Pan et al.,[14] who have demonstrated a full-field high-temperature deformation measurement at 1200°C using DIC. Pankow et al.[15] developed a method that measures out-of-plane displacement using 3-D DIC with a single high-speed camera, and stated that the benefits of this method included reduced cost of equipment and elimination of issues related to image synchronization when multiple high-speed cameras are used.

The advantages of white-light illumination and simplicity of surface preparation make DIC rather popular in experimental mechanics. By taking advantage of speckle correlation principles used in DIC, a full-field methodology called digital gradient sensing (DGS) has been proposed more recently for measuring two orthogonal small angular deflections of light rays.[16,17] The two variants of DGS, a transmission-mode DGS (t-DGS) for measuring stress gradients in transparent solids and a reflection-mode DGS (r-DGS) for measuring surface slopes on optically reflective objects, have been demonstrated to study both quasistatic and dynamic problems by its inventors. Hao et al.[18] have followed up with a report investigating fiber pull-out problem using t-DGS. Zhang et al.[19] applied r-DGS to measure surface

*Address all correspondence to Hareesh V. Tippur, E-mail: tippuhv@auburn.edu

0091-3286/2019/$25.00 © 2019 SPIE

topography and thin film stresses at elevated temperatures. Jain and Tippur[20] extended r-DGS to study transient deformations and damage in planar solids. Dai et al.[21] evaluated the thermal residual stress distribution in a transparent specimen using lateral shearing interferometry and t-DGS, and concluded that t-DGS is more practical relative to the interferometric counterpart. Miao et al.[22] demonstrated the feasibility of coupling r-DGS with a robust 2-D integration scheme called higher-order finite-difference-based least-squares integration (HFLI) to measure the surface topography of thin structures. Later on, Miao and Tippur[23,24] also showed that the approach can be used to study the problem of a composite plate subjected to dynamic out-of-plane impact to extract submicron scale deformations around impact region using ultrahigh-speed (1 Mfps) photography. The authors also reported their successful attempts to further increase the measurement sensitivity of DGS methods[25] to potentially extend these methods to study fracture and failure of high stiffness and low toughness ceramics and glasses. Although the authors have reported that submicron deformation can be measured by using r-DGS and HFLI, questions pertaining to the smallest measurable deformation and its accuracy are yet to be quantified. Accordingly, the current investigation is a step toward answering these questions.

In the following, the experimental details and working principle of r-DGS and HFLI are briefly introduced. Then, the smallest measurable out-of-plane deformation in dynamic and static experiments is separately explored. Finally, the major results of this study are summarized.

2 Optical Methodology

The schematic of the experimental setup for r-DGS to measure surface slopes is shown in Fig. 1. A digital camera is used to record random speckles located on a target plane via the reflective specimen surface. To accomplish this, the specimen and the target plate are placed perpendicular to each other, and the beam splitter is positioned at 45 deg relative to the specimen and target plate. The target plate has spray painted random black and white speckles, and is uniformly illuminated using a broad spectrum (white) light. The specimen surface is made reflective by depositing aluminum film. When the specimen is in its undeformed state, the gray scale at a generic point P on the target plate is recorded by a camera pixel through point O on the specimen plane. Thus, recorded gray scales by all the pixels constitute a reference speckle image. After the specimen suffers deformation due to the applied load or changes its state after a time-lapse, the gray scale at a neighboring point of P, namely Q on the target plate, is photographed by the same pixel through the same point O on the specimen surface. The corresponding image of the specimen in the deformed state is recorded next. The "local" orthogonal speckle displacements identified as $\delta_{x;y}$ in Fig. 2 can be obtained by performing a 2-D correlation of the speckle images in the reference and deformed states. The corresponding angles $\phi_{x;y}$ representing two orthogonal angular deflections of light rays can then be obtained, as shown in Fig. 2.

For simplicity, only the angular deflections of light rays in the $y-z$ plane are shown in Fig. 2. Here, OQ makes an angle ϕ_y with OP. Further, $\phi_y = \theta_i + \theta_r$, where θ_i and $\theta_r (= \theta_i)$ are incident and reflected angles relative to the normal to the specimen and $\underline{n}$ denotes the local normal to the deformed surface. A similar relationship in the $x-z$ plane can be obtained as well. Then, the two orthogonal surface slopes of the surface can be related to $\phi_{x;y}$ as $\frac{\partial w}{\partial x;y} = \frac{1}{2}\tan(\phi_{x;y})$. The governing equations for r-DGS are as follows:[17]

$$\frac{\partial w}{\partial x;y} = \frac{1}{2}\tan(\phi_{x;y}) \approx \frac{1}{2}(\phi_{x;y}) \approx \frac{1}{2}\left(\frac{\delta_{x;y}}{\Delta}\right), \tag{1}$$

where Δ is the distance or the gap between the specimen and target planes, and approximately small angle is used. It is important to note that the coordinates of the specimen plane are utilized for describing the governing equations and the camera is focused on the target plane during photography. Therefore, coordinate mapping is needed to transfer the target plane locations to the specimen plane. This can be done by adopting the pin-hole camera approximation, $(x;y) = \frac{L}{L+\Delta}(x_0;y_0)$, where $(x;y)$ and $(x_0;y_0)$ represent the coordinates of the specimen and target planes, respectively, and L is the distance between the specimen and the camera.[16]

The two orthogonal surface slopes obtained from r-DGS can be numerically integrated to reconstruct the surface

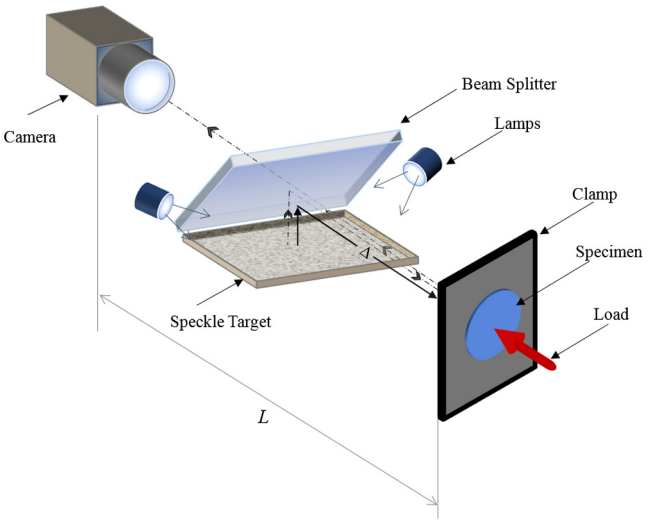

Fig. 1. Schematic of r-DGS experimental setup.

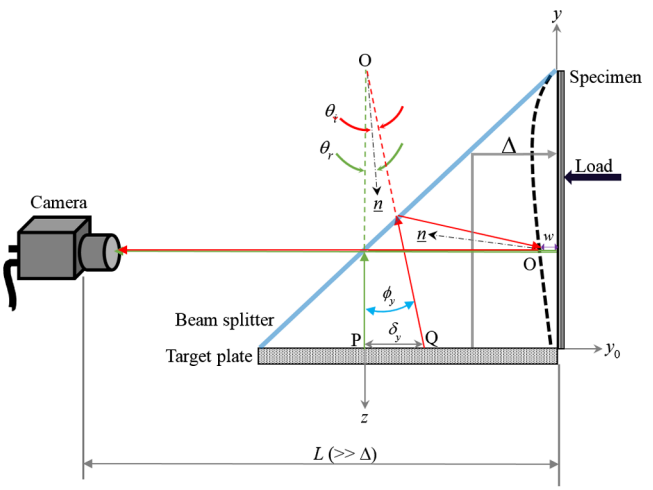

Fig. 2. Working principle of r-DGS.[22]

topography. This reconstruction can be carried out using 2-D integration based on finite-difference method. The integration method used in this paper is called the HFLI method.[26] The details for algorithms of HFLI can be found in Refs. 22 and 23.

3 Ultrahigh-Speed Measurements

First, an experiment to measure out-of-plane deformations of an impact loaded soda-lime glass plate, a low-toughness, and high-stiffness material, monitored using r-DGS in conjunction with ultrahigh-speed single sensor digital camera was undertaken. A 152.4 mm × 101.6 mm rectangular specimen of 4.6-mm thickness was used. One of the two 152.4×101.6 mm^2 faces was coated with aluminum film using vapor deposition technique to make the surface reflective. The schematic of the experimental setup used is shown in Fig. 3. A modified Hopkinson pressure bar (or simply a "long-bar") was used for loading the uncoated backside of the specimen. The long-bar was a 1.83-m steel rod of 25.4-mm diameter with a tapered flat end of 3-mm diameter kept in contact with the specimen. A 305-mm long, 25.4-mm diameter steel striker placed in the barrel of a gas-gun was coaxially aligned with the long-bar at the start of the experiment. The striker was launched toward the long-bar at a low velocity of ∼2.5 m/s during the test. The specimen was clamped using a fixture containing two steel plates with circular apertures, see Fig. 3. The 63.5-mm diameter apertures were coaxial allowing optical observations within this region. The loading was at the center of the aperture. A beam splitter and the speckle target plate were placed in a 45-deg holder, housed within the specimen holding fixture so that the speckle pattern on the target plate was viewed via the reflective face of the specimen. The deformations on the front face of the specimen were photographed by a Kirana-05M ultrahigh-speed digital camera assisted by a pair of high-energy flash lamps (Cordin model 659) to illuminate the target. The ultrahigh-speed camera is a 924×768 pixels single sensor camera, capable of recording 180, 10-bit images at a maximum rate of up to 5 million frames per second (fps). The camera and the two flash lamps were triggered using a variable delay circuit relative to the striker impacting the long-bar and the duration required for the stress waves to travel the length of 1.83 m along the steel rod.

A Nikon 70- to 300-mm focal length zoom lens with an adjustable bellows was used with the camera to record the images. A good exposure and focus were achieved by stopping down the lens aperture to F#8 after focusing on the speckles. The distance between the specimen and the camera lens (L) was ∼950 mm and the one between the specimen mid-plane and the target plane (Δ) was 102 mm. A total of 180 images, some in the undeformed and others in the deformed states of the specimen, were recorded at 1.25 million fps (interframe period 0.8 μs). When the long-bar was impacted by the striker, a 1-D compressive stress wave was generated that propagated along the length of the long-bar. The fixture used to house the specimen was mounted on a pair of rails so that it can travel away from the long-bar when the specimen was loaded. However, the inertia of the fixture was substantially higher than that of the specimen and hence, it took several milliseconds for the fixture to move away from the long-bar while the images of the deformed specimen were recorded for ∼50 μs. One undeformed image before the start of deformation was selected as the reference image ($t = 0$ μs). Subsequent images were correlated with that reference image using ARAMIS® image analysis software. During correlation, a subimage size of 25×25 pixels (1 pixel corresponds to 83.68 μm on the specimen) with 15 pixels overlap was adopted to extract the local displacements $\delta_{x;y}$ in the region-of-interest (ROI).

The time-resolved orthogonal surface slope contours of $\frac{\partial w}{\partial x}$ and $\frac{\partial w}{\partial y}$ due to transient stress wave propagation in the glass plate are shown in Fig. 4 at a few select time instants. In the early stages of impact, deformations are concentrated close

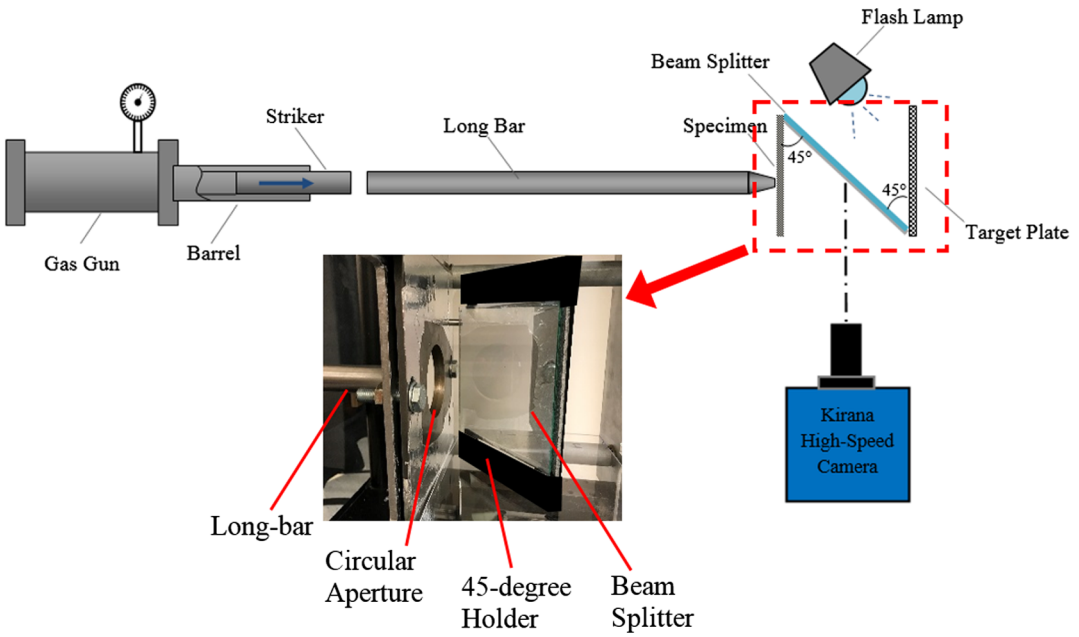

Fig. 3. Schematic of the experimental setup for dynamic plate impact study. Inset shows the close-up of the optical arrangement.

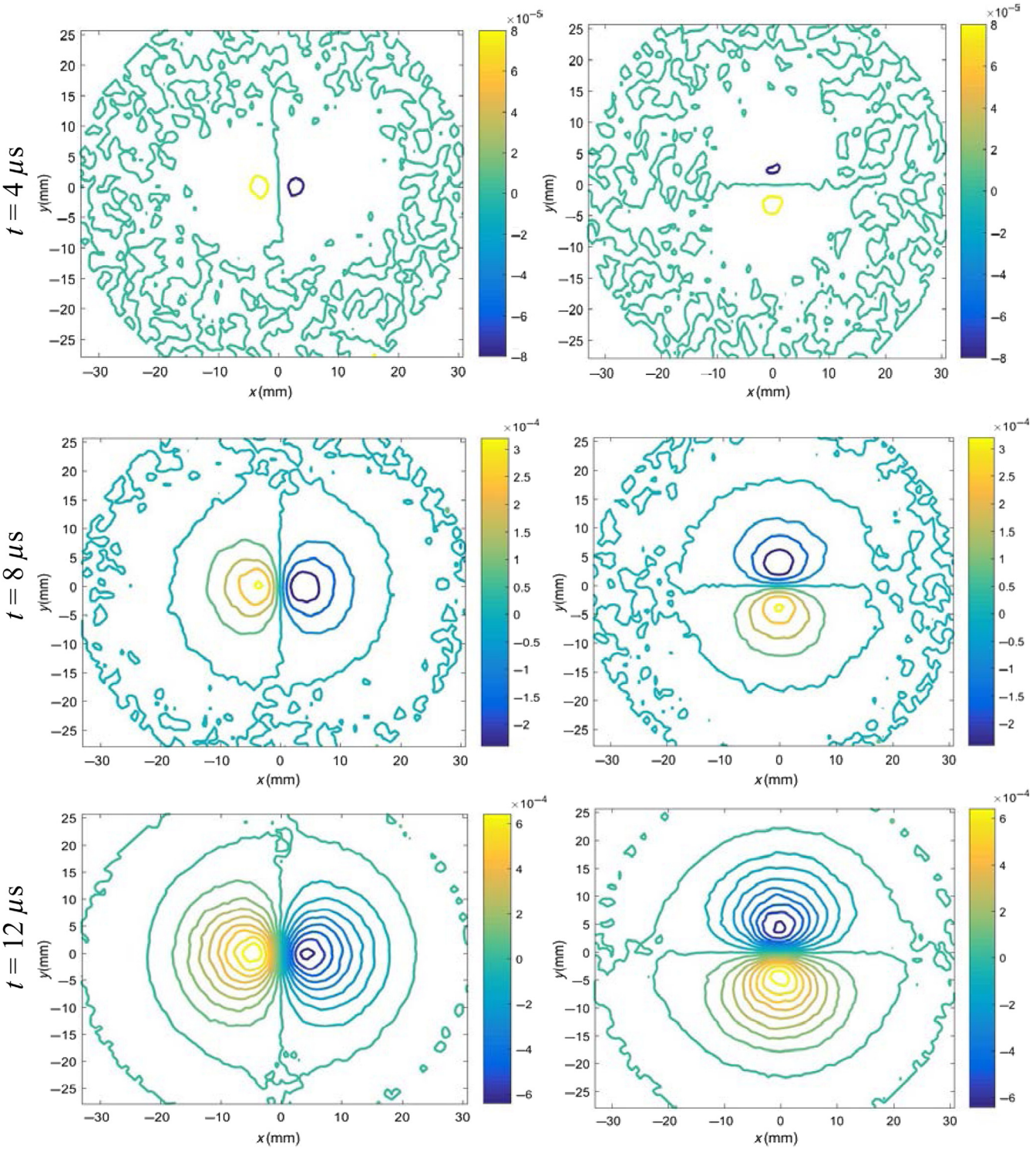

Fig. 4. Evolution of surface slope $w_{,x}$ (left column) and $w_{,y}$ (right column) contours for a clamped glass plate subjected to central impact. Note: (0, 0) is made to coincide with the impact point. Contour increments $= 8 \times 10^{-5}$ rad.

to the center of the plate resulting in small surface slope contours. With the passage of time, the contours get denser and larger near the contact point. The symmetry in the magnitude of these contours (of opposite sign) about the x- and y-axes at different time instants follows the theoretical predictions of propagating flexural waves in a thin structure. The reconstructed 3-D surfaces computed from 2-D integration using surface slope data from r-DGS in conjunction with HFLI algorithm are plotted in Fig. 5. The corresponding contours of out-of-plane displacements (w) at 0.5-μm increment are shown in the right column of Fig. 5. The out-of-plane deformation is $\sim$0.63 μm at $t = 4$ μs, which shows that this method can indeed detect submicron deformations at submicrosecond intervals. The circular contours in the

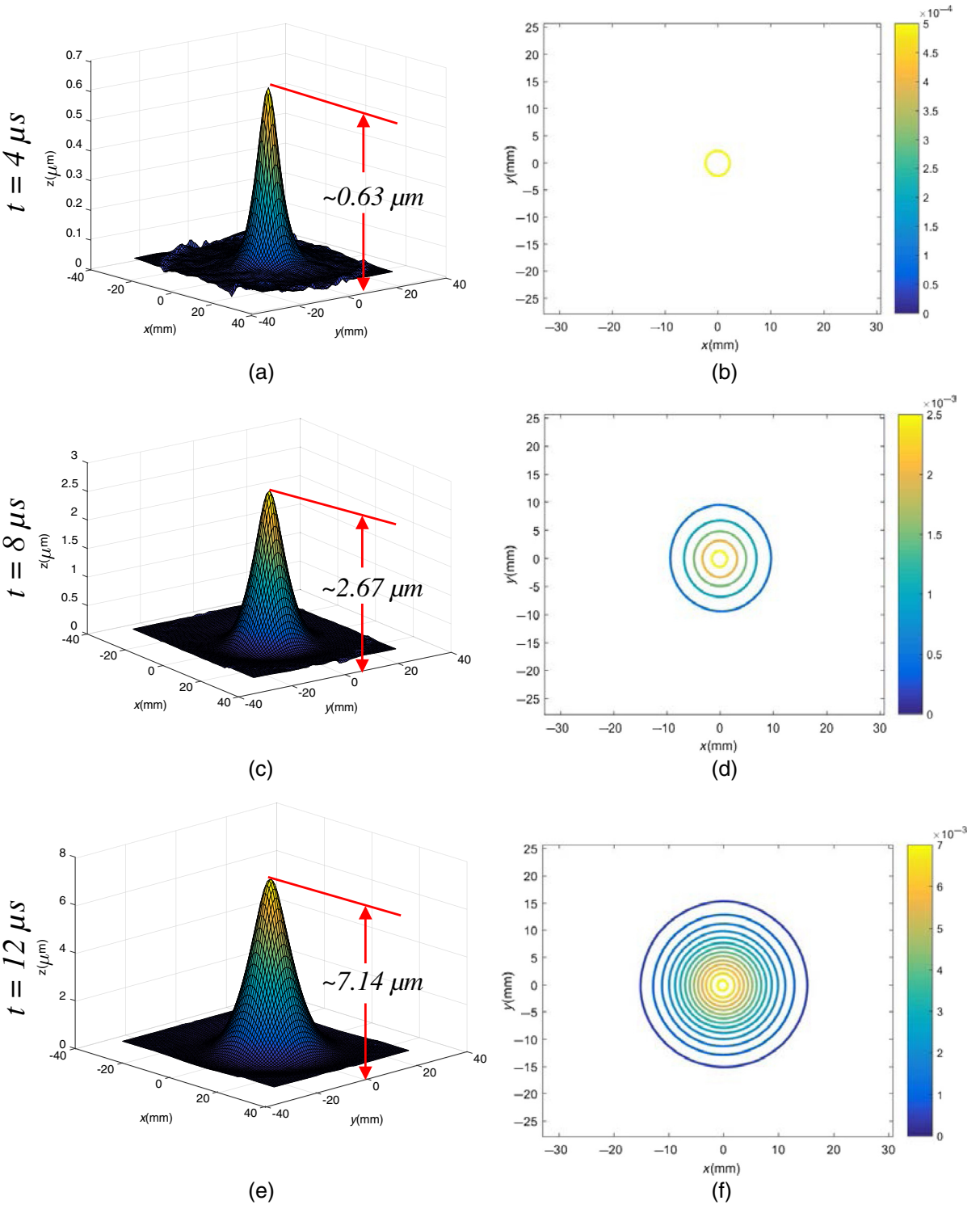

Fig. 5. Measured surface topography of glass plate at a few select time instants. (a)–(c) Reconstructed 3-D surface using HFLI. (d)–(f) Out-of-plane displacement (w) contours (0.5-μm increment). Note: (0, 0) is made to coincide with the impact point.

right column demonstrate that the reconstructed shape matches well with the reality of the experiment qualitatively. The out-of-plane deformation along the diameter $x = 0$ at a few selected time instants is plotted in Fig. 6. The radius R here is measured from the impact point (0, 0). With the passage of time, the out-of-plane deformations expand outward from the impact point toward the outer clamped edge of the plate while the overall amplitude of deformation increases at the impact point.

3.1 *Smallest Measurable Out-of-Plane Deformation*

As stated previously, r-DGS measurements performed at ultrahigh recording speeds along with the HFLI approach

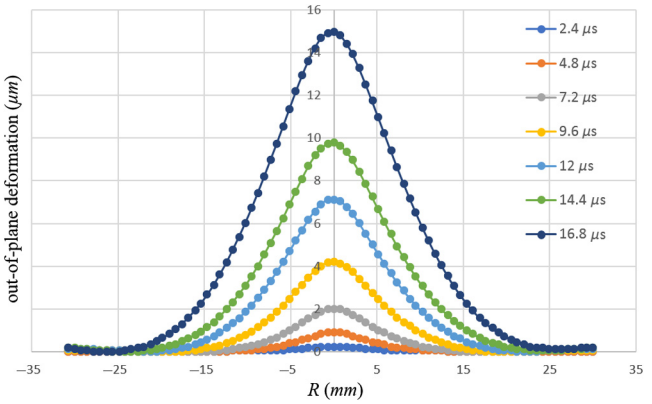

Fig. 6. The measured profiles for a clamped glass plate subjected to central impact.

are able to detect submicron scale deformations at submicrosecond intervals during a stress wave loading event over a large 62.5-mm diameter, field-of-view (FOV). Therefore, it is pertinent that the smallest measurable out-of-plane deformation be quantified to justify the validity of such measurements. Two aspects were considered for validating these observations; one was based on an accepted estimate of the smallest measurable displacement from the prevailing 2-D DIC algorithms, and the other was by correlating two speckle images in the undeformed state but recorded by the camera with a time lapse. The latter provided a good estimate of measurement noise due to the combined effect of electronic noise of the imaging device as well as the measurement environment (e.g., random vibrations, thermal currents in the optical path, etc.).

3.1.1 *Method-1*

Since r-DGS utilizes 2-D DIC to measure speckle displacement to evaluate angular deflections of light rays, the measurement accuracy of DIC algorithm directly affects that of DGS. It is widely accepted[13] that the smallest measurable in-plane displacement of speckles from popular DIC algorithms is ~1% of one pixel of the image. Accordingly, to be conservative, 2% of one image pixel dimension was assumed in this work as the smallest measurable in-plane displacement of speckles from DIC to assess the accuracy of r-DGS. That is, in the experiments described earlier, as 1 pixel corresponded to 83.68 μm on the target plane, the smallest measurable in-plane displacement, δ, was $\approx 1.67 \times 10^{-6}$ m. The corresponding surface slope under small angle approximation being $\frac{\delta}{\Delta}$, where $\Delta = 119$ mm is the length of the optical-lever of the setup. Therefore, the smallest measurable angular deflection was $\approx 1.4 \times 10^{-5}$ rad at the center of the subimage (or the facet). In this experiment, the subimage overlap or facet step was 10 pixels. Hence, the distance between two neighboring subimage centers, d_x, was $\approx 8.37 \times 10^{-6}$ m. Recognizing that $w_{,x} \approx \frac{w_i \sim w_{i+1}}{d_x}$ for two neighboring data points, the smallest out-of-plane deformation, w, based on the trapezoidal rule-of-integration was $w = (1.4 \times 10^{-5}) \times (83.68 \times 10^{-5})$ m or 11.7 nm.

Under the assumption of plane stress conditions and using Hooke's law, the out-of-plane deformation can be related to in-plane normal stresses as follows:

$$w \approx -\frac{vB}{2E}(\sigma_{xx} + \sigma_{yy}), \tag{2}$$

where ν is the Poisson's ratio, B is the undeformed thickness, and E is the elastic modulus of the specimen. Hence, the smallest measurable $(\sigma_{xx} + \sigma_{yy})$ can be obtained from the smallest measurable w. For a 4.6-mm thick soda-lime glass, using nominal values of elastic constants $\nu = 0.22$, $E = 70$ GPa, the smallest measurable $(\sigma_{xx} + \sigma_{yy}) \approx 1.6$ MPa.

3.1.2 *Method-2*

The second method for estimating the smallest measurable w was to correlate two speckle images in the undeformed state recorded by the ultrahigh-speed camera with a submicrosecond time lapse. Figure 7 shows two such randomly selected speckle images. Therefore, ideally, the in-plane displacements obtained by correlating these two images should be zero. However, due to various experimental deficiencies, such as electronic noise of the imaging system, random vibrations, thermal fluctuations, and shortcoming of the correlation algorithm, the in-plane speckle displacements extracted will not be zero. The corresponding slopes thus obtained after dividing the in-plane displacements by the optical-lever Δ will be affected as well. A pair of surface slope components of angular deflections is shown in

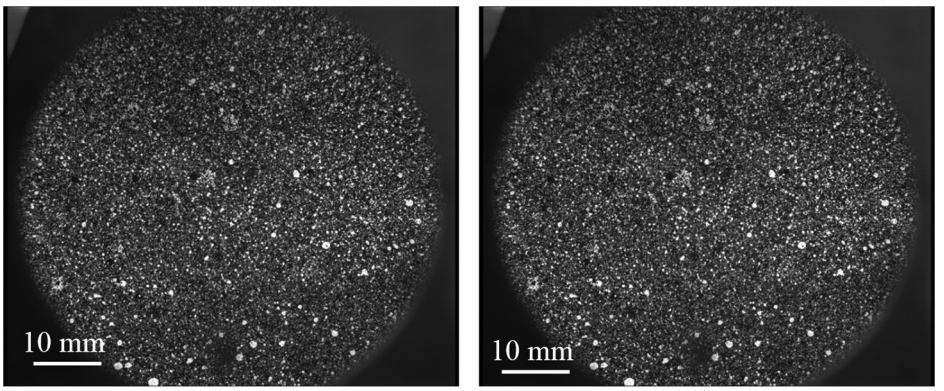

Fig. 7. (a) and (b) Two select speckle images recorded by the ultrahigh-speed camera in the undeformed state (or two reference images recorded with a time lapse).

Fig. 8. The contour increments here were intentionally kept very small, 1×10^{-5} rad (eight times smaller than the one in Fig. 4, and above the 1% of the pixel limit of DIC), so that the slope contours obtained from noise could be observed. The red dot in Fig. 8 indicates the impact point or the origin corresponding to row 38, column 45 of the processed 74×88 data array. It can be observed from Fig. 8 that the slope values are very small and vary randomly, whereas they are relatively large along the edges, highlighting the edge effects along the periphery of the specimen.

To quantify the noise level better, the horizontal slope along three rows and three columns, inclusive of the origin, was extracted and plotted in Fig. 9. It should be noted here that five data points at the two ends of the diameter were removed from the plot as they are close to the specimen/image edges containing much higher noise levels, not representative of the methodology itself. It can be observed from Fig. 9 that most of the noise is spread within $\pm 2 \times 10^{-6}$ rad range, suggesting that r-DGS is capable of detecting angular deflections of light rays or surface slopes in the range of microradians.

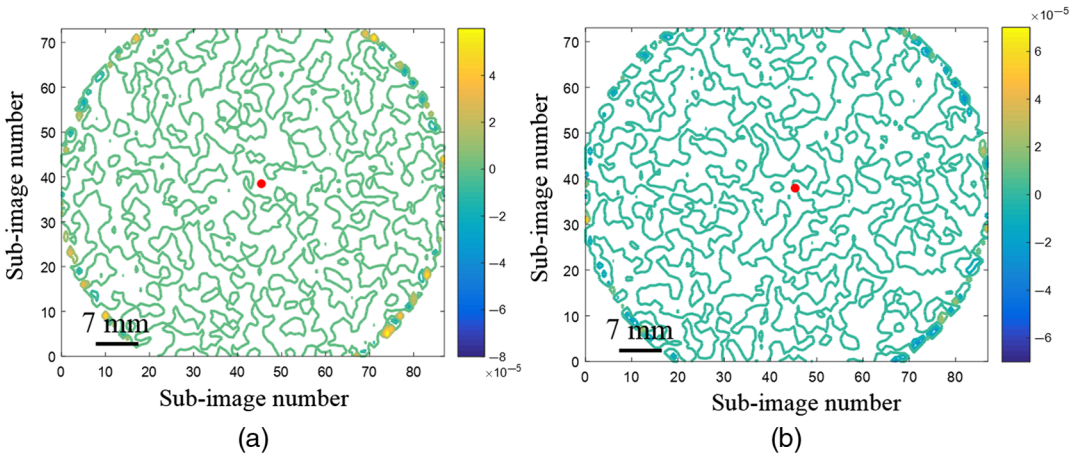

Fig. 8. Surface slopes (a) $w_{,x}$ and (b) $w_{,y}$ contours. Contour increments $= 10 \times 10^{-6}$ rad. Impact point: row 38, column 45.

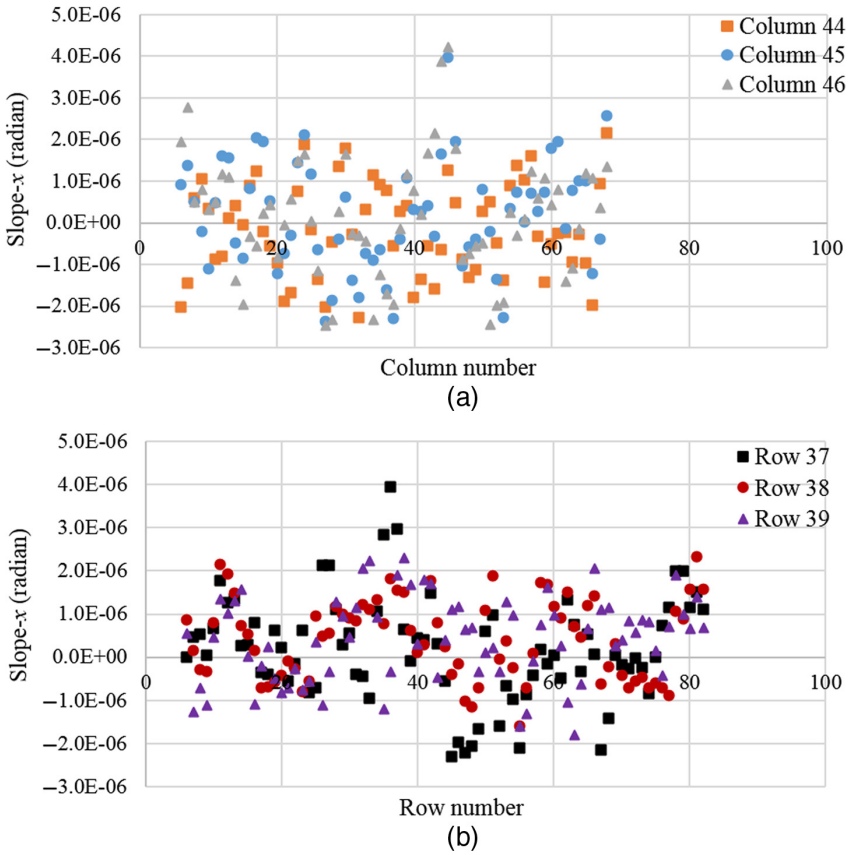

Fig. 9. Slopes in the horizontal direction (a) along three neighboring columns and (b) along three neighboring rows. The rows and columns are along the horizontal and vertical diameters in Fig. 8.

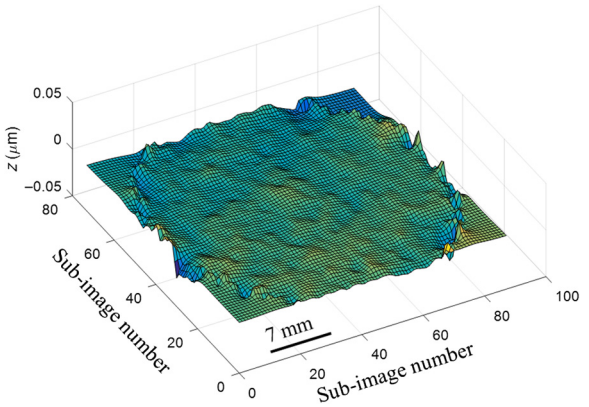

Fig. 10. Reconstructed surface topography showing spurious out-of-plane displacement obtained by correlating two speckle images recorded by the ultrahigh-speed camera and postprocessed using HFLI algorithm.

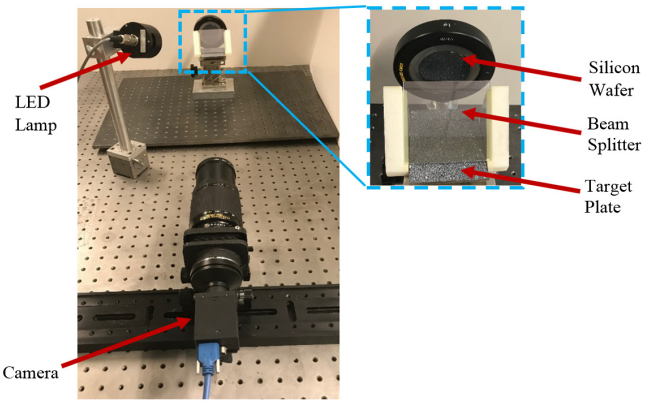

Fig. 12. Experimental setup for performing r-DGS measurements under quasistatic conditions. Inset shows close-up of the optical arrangement.

The surface slopes such as the ones shown in Fig. 8 were numerically integrated using HFLI algorithm to obtain the topographic information of the surface and is shown in Fig. 10 as a 3-D surface plot. The units of the vertical axis in Fig. 10 are plotted as μm, whereas the two horizontal axes are in the matrix array format corresponding to the ones shown in Fig. 8. It can be observed from Fig. 10 that the reconstructed surface is textured and "rough" in appearance and the noise along the edge is relatively large. Note that the algorithmic error of HFLI is included in the noise. Hence, the surface topography obtained here contains three noise contributors, namely the experimental apparatus including the imaging system, the speckle correlation, and integration algorithms. The out-of-plane deformation along the three rows and three columns inclusive of the origin is again

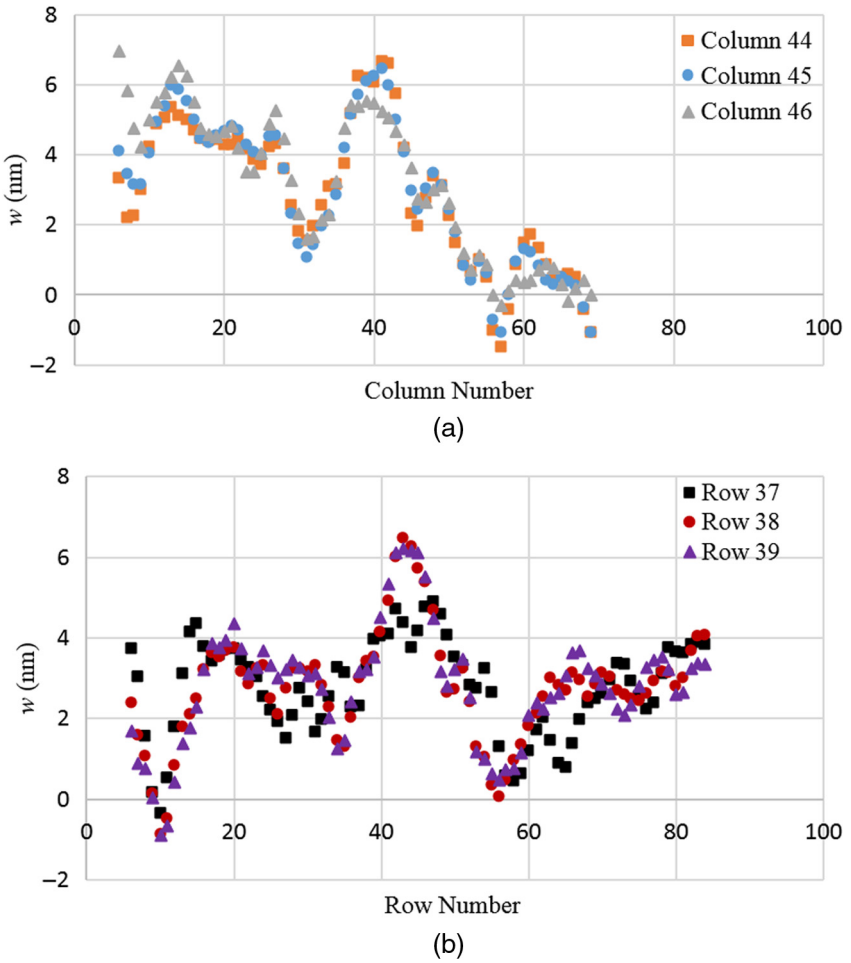

Fig. 11. (a) Spurious nanoscale out-of-plane displacements along three neighboring columns and (b) three neighboring rows under dynamic recording conditions.

extracted and plotted in Fig. 11. Once again, five data points at the two ends have been truncated in this plot. It can be observed from Fig. 11 that the largest noise value, w, is ~7 nm. Based on Hooke's law and plane stress approximation, the corresponding $(\sigma_{xx} + \sigma_{yy})$ is ~1 MPa. These values are in the same range as the ones obtained from method-1 discussed earlier. Thus, it can be concluded that, under dynamic experimental conditions, with microsecond time lapse period, the smallest measurable w from r-DGS with HFLI is ~10 nm over a large FOV using the current state-of-the-art imaging equipment.

4 Smallest Measurable Deformation: Quasistatic Conditions

Miao et al.[22] have previously demonstrated the feasibility of r-DGS used in conjunction with HFLI to map surface

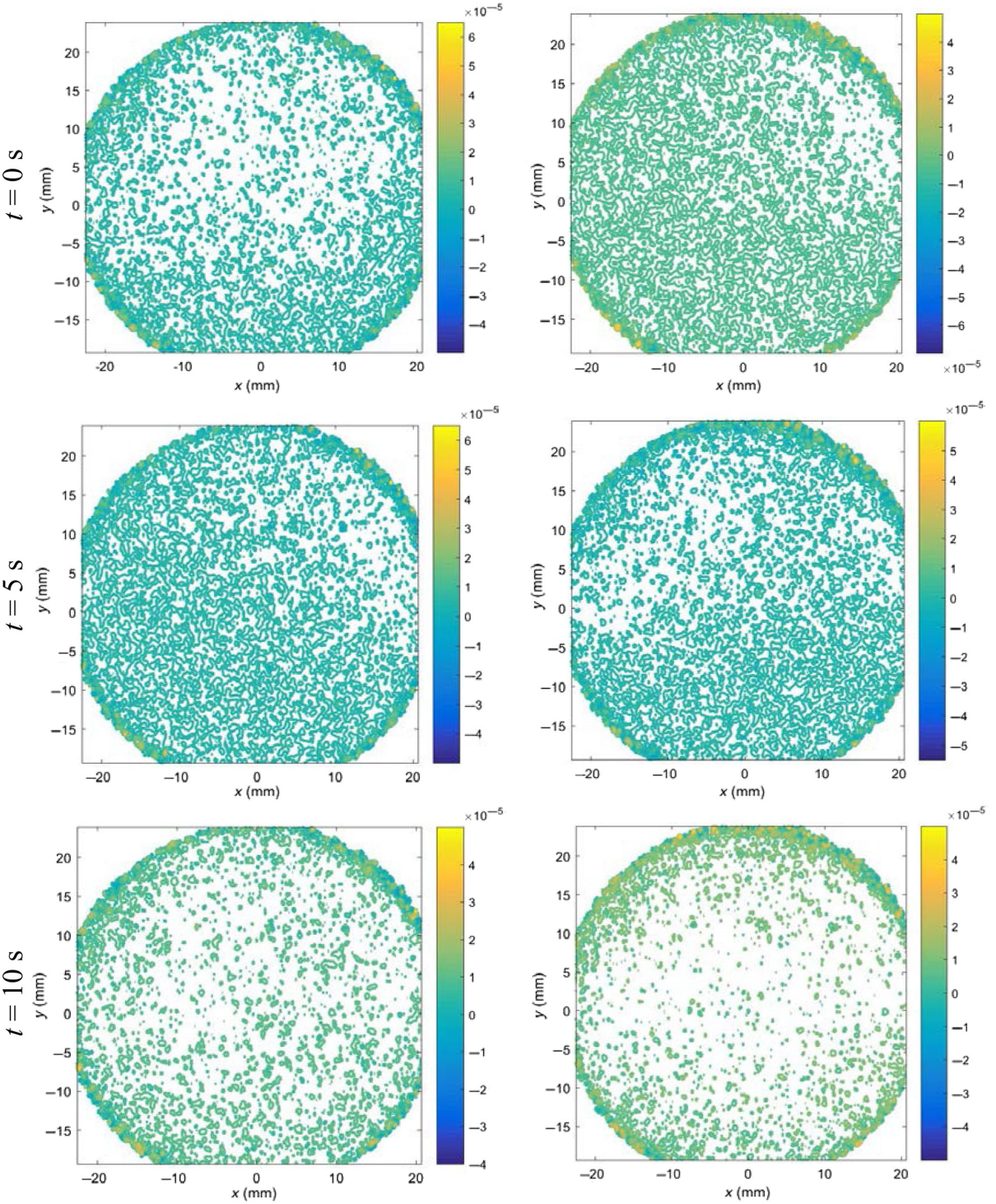

Fig. 13. Spurious surface slopes $w_{,x}$ (left column) and $w_{,y}$ (right column) for clamped silicon wafer recorded at 0.2 fps. Note that (0, 0) is made to coincide with the center of silicon wafer. Contour increments $= 5 \times 10^{-6}$ rad.

topography of a clamped reflective silicon wafer subjected to out-of-plane concentrated load. The work showed that the measured values deviated by ~5% of the expected values during quasistatic, manual loading of the wafer using a screw-type micrometer device. However, that work did not provide details on the smallest measurable out-of-plane deformation. Accordingly, the experiments were repeated to assess the smallest measurable deformation under static loading conditions. The experimental details are as follows.

A single-face polished, silicon wafer of diameter 50.8 mm and 360 μm thickness was used. (Note that any planar reflective specimen/substrate should suffice for this work but an existing setup was utilized for convenience.) The unpolished face was bonded to a thick steel washer with a circular aperture of 30 mm using a slow curing epoxy adhesive. The steel washer was secured in a cylindrical holder. A target plate, decorated with random black and white speckles, was placed at 90 deg to the silicon wafer. Two LED lamps were used to

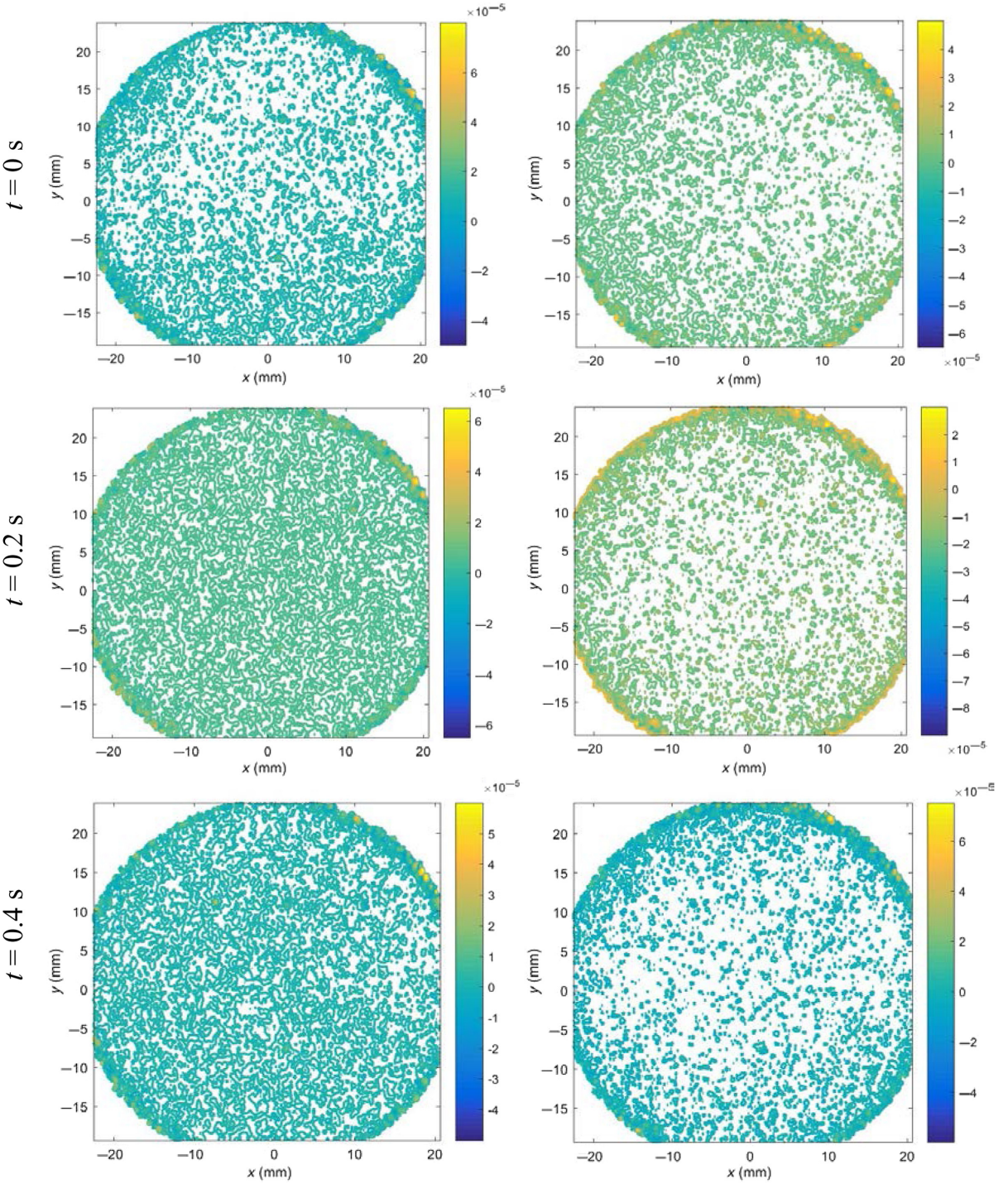

Fig. 14. Spurious surface slopes $w_{,x}$ (left column) and $w_{,x}$ (right column) for clamped silicon wafer recorded at 5 fps. Note that (0, 0) is made to coincide with the center of silicon wafer. Contour increments $= 5 \times 10^{-6}$ rad.

illuminate the speckle pattern on the target. A beam splitter was placed at 45 deg to both the silicon wafer and the target plate (see Fig. 12). The distance between the silicon wafer surface and the target plate (Δ) was 112 mm. A point gray digital camera with a Nikon 70 to 300 mm lens and adjustable bellows was used to record speckles on the target plate through the beam splitter via the reflective silicon wafer surface. The distance between the silicon wafer and the lens (L) was ~1445 mm.

First, when the silicon wafer was under no-load condition, the speckle images (2048×2048 pixels) were recorded at two different rates, 0.2 and 5 fps. One of the images in each experiment was selected as the reference image ($t = 0$ μs), and the rest of the images were correlated with that reference

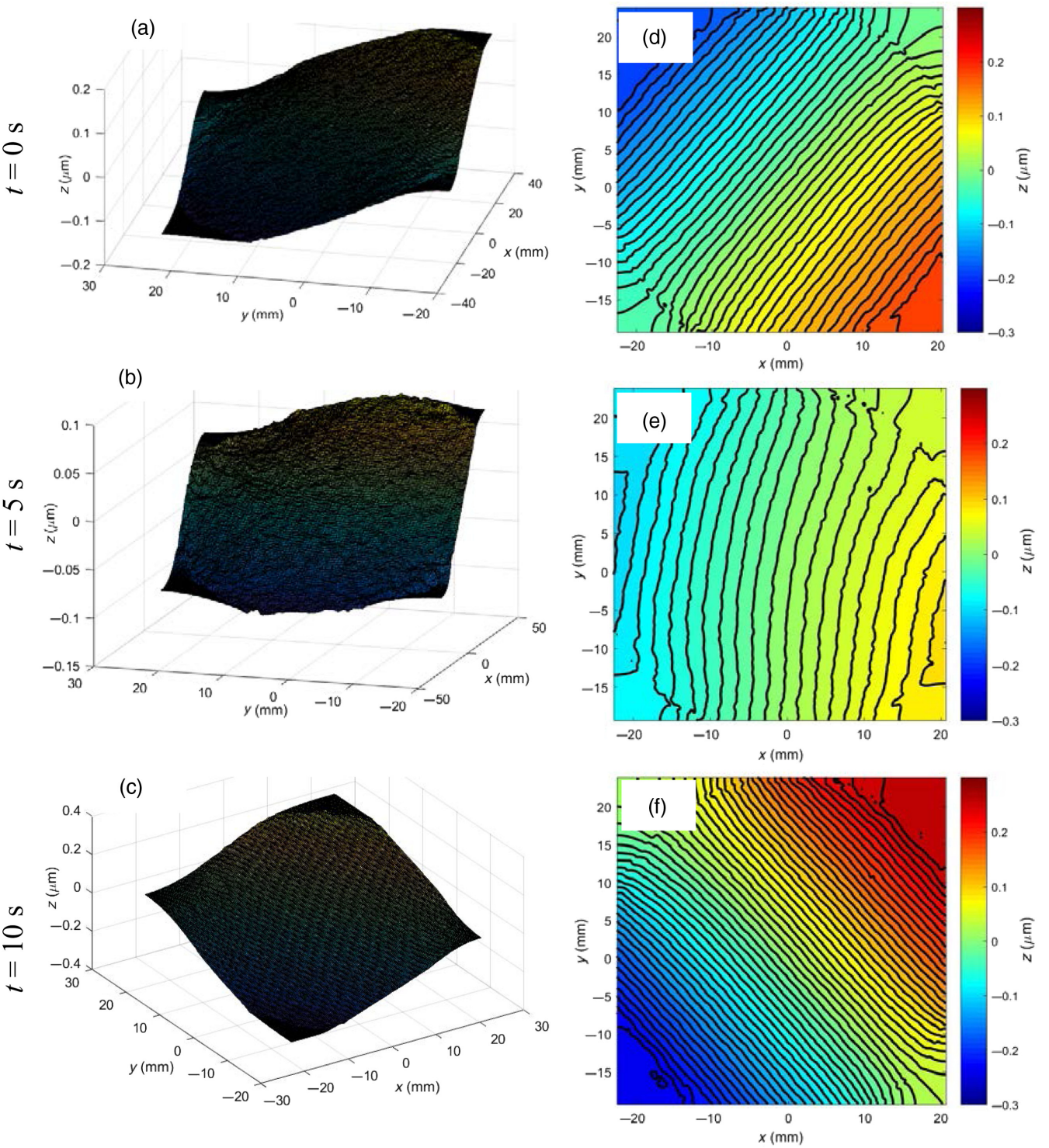

Fig. 15. Spurious surface topography obtained from integrating surface slopes using HFLI method for a clamped silicon wafer recorded at 0.2 fps. (a)–(c) 3-D surface. (d)–(f) Out-of-plane displacement (w) contours (0.01-μm increments).

using ARAMIS® image analysis software. During correlation, a subimage size of 25×25 pixels (1 pixel $= 23.16$ μm of the speckle image) with 15 pixels overlap was used to extract the local displacement of speckles $\delta_{x;y}$ in the ROI.

The time-resolved orthogonal surface slope contours of $\frac{\partial w}{\partial x;y}$ are plotted in Figs. 13 and 14 corresponding to framing rates of 0.2 and 5 fps, respectively. Since the silicon wafer was not subjected to any load at all during this experiment, the surface slopes should be uniformly zero in the ROI. However, due to experimental noise, the nonzero slopes evidently occur throughout the ROI. The contour increments here are 5×10^{-6} rad; as a result, extremely small slopes can be observed. The random slopes are spread in $\pm 3 \times 10^{-6}$ rad range.

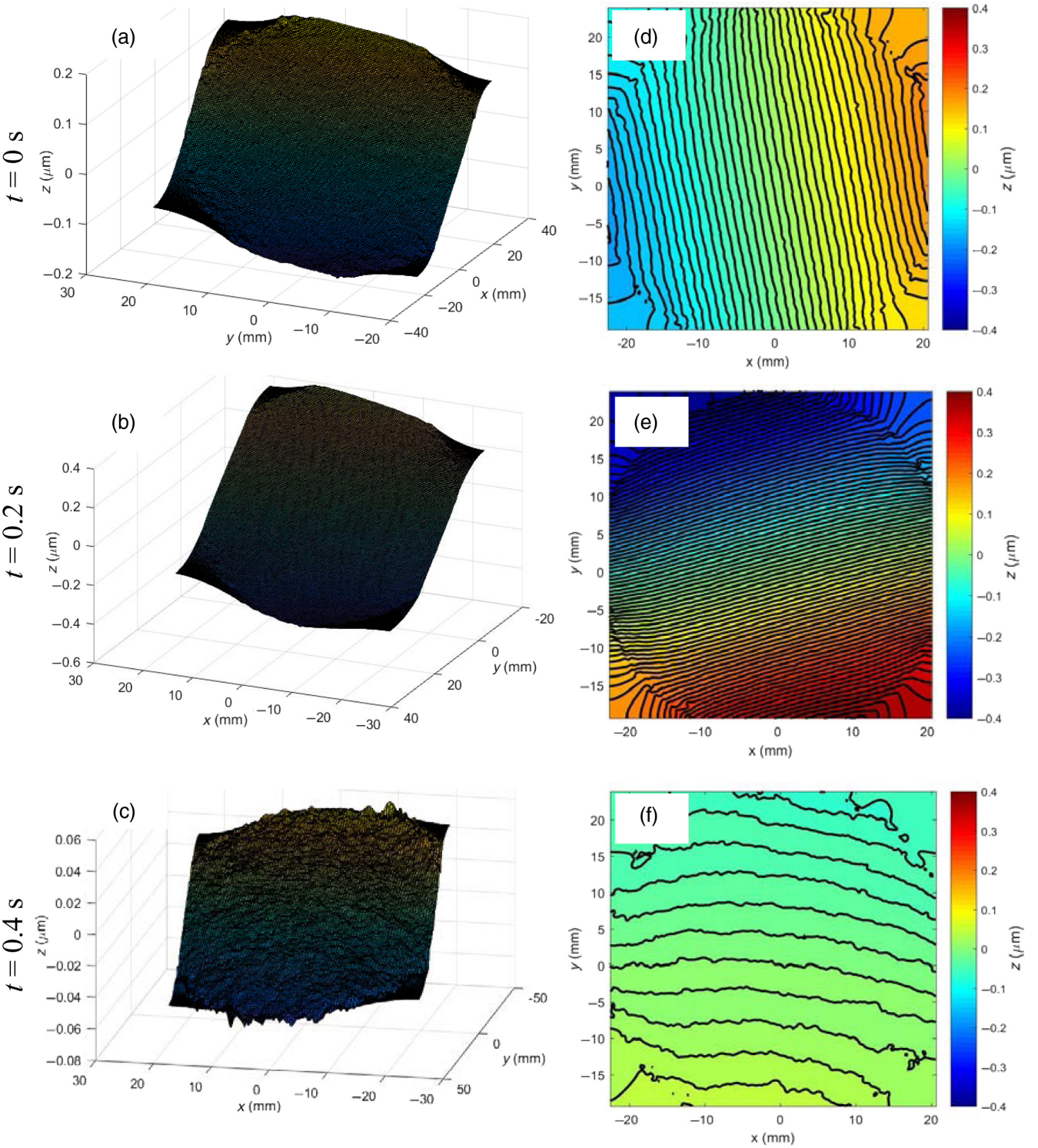

Fig. 16. Spurious surface topography obtained from integrating surface slopes using HFLI method for a clamped silicon wafer recorded at 5 fps. (a)–(c) 3-D surface. (d)–(f) Out-of-plane displacement (w) contours (0.01-μm increments).

The surface slopes in Figs. 13 and 14 were numerically integrated using the HFLI algorithm to obtain the instantaneous surface topography and are plotted in Figs. 15 and 16, respectively. The left columns in these figures represent the reconstructed surfaces at different time instants, the right columns show the out-of-plane displacement (w) contours corresponding to the 3-D surfaces in the left columns. (The 3-D surfaces in Figs. 15 and 16 are plotted from different azimuth angles to best present the surface characteristics.) It should be noted that the scales of the horizontal axes are in mm scale, whereas the vertical axes are in μm. Accordingly, all the 3-D surfaces plotted here appear planar but inclined, although ideally, they should be without any tilt or devoid of contours. The contour increments for the out-of-plane displacement (w) in the right column are set at 0.01 μm or 10 nm. The texture (roughness) of the reconstructed surface due to experimental noise can be observed from the wrinkles on each contour. The out-of-plane displacement (w) contours better reveal the phenomenon that all the 3-D surfaces are tilted in different spatial directions. This is noticeably different from the reconstructed "flat" surface of the dynamic counterpart shown in Fig. 10. It is worth noting that the laboratory where these experiments were performed was located on the top floor of a four-story building, in close proximity to a passenger elevator, the mechanical vibrations expectedly influence the time lapse photography in addition to the electronic noise and thermal currents in the optical path. Considering the measurement in the dynamic counterpart was in the nanometer range over a large FOV using a much shorter interframe period (0.8 μs), the role of mechanical vibrations in the slow-speed, static experiment is significantly higher. The fact that the reconstructed surfaces are arbitrarily tilted in space at the instant of recording matches the reality that random mechanical vibrations affected the time lapse measurements. Evidently, the smallest out-of-plane deformation ranges from -0.06 to 0.06 μm in Figs. 16(c) and 16(f), whereas the spread is within -0.4 to 0.4 μm in Figs. 16(b) and 16(e). Note that the higher errors at 5 fps when compared to 0.2 fps further emphasize the effect of random vibrations at lower imaging speeds influencing the measurements. This also indicates that the r-DGS is able to measure out-of-plane deformation in the submicron range over a relatively large FOV even under quasistatic conditions without special vibration isolation of the apparatus.

5 Conclusions

In this paper, the accuracy of out-of-plane deformations measured from r-DGS used in conjunction with HFLI is discussed. First, the feasibility of detecting deformations over a large FOV is demonstrated using ultrahigh-speed submicrosecond digital photography with sub microsecond time lapse. Next, the validity of those measurements is justified using two methods, one is based on the smallest measurable displacement from 2-D DIC and the other by correlating two speckle images recorded in the undeformed state with a time lapse. The verification shows that the smallest measurable out-of-plane deformation is ~10 nm using ultrahigh-speed photography at 10^6 fps. On the other hand, when using slow-speed photography, 10^1 fps, the smallest measurable out-of-deformation was much higher but still in the submicron range over a large FOV. The difference between ultrahigh-speed photography and slow-speed photography revealed combined effects of random mechanical vibrations and thermal currents in the optical path. The accuracy of measurement decreased (from ~10 nm to 0.4 μm error) in slow-speed, quasistatic experiments. Hence, it could be concluded that the application of r-DGS with HFLI is able to measure nanoscale deformations provided errors from mechanical vibrations and thermal currents are avoided using minimum time lapse during image capture. Considering the simplicity of the experimental setup, and digital recording and postprocessing steps, the potential of this approach to optical metrology of planar substrates (e.g., silicon wafer used in the semiconductor industry) is enormous.

Acknowledgments

Equipment support for this research from Army Research Office grant W911NF-15-1-0357 (DURIP) is gratefully acknowledged.

References

1. S. Ettl et al., "Shape reconstruction from gradient data," *Appl. Opt.* **47**, 2091–2097 (2008).
2. F. Chen, G. M. Brown, and M. Song, "Overview of three-dimensional shape measurement using optical methods," *Opt. Eng.* **39**(1), 10–22 (2000).
3. H. Ding et al., "Warpage measurement comparison using shadow moiré and projection moiré methods," *IEEE Trans. Comp. Packag. Technol.* **25**, 714–721 (2002).
4. B. Han and Y. Guo, "Thermal deformation analysis of various electronic packaging products by moiré and microscopic moiré interferometry," *J. Electron. Packag.* **117**, 185–191 (1995).
5. J.-H. Park et al., "A study of hygrothermal behavior of ACF flip chip packages with moiré interferometry," *IEEE Trans. Comp. Packag. Technol.* **33**, 215–221 (2010).
6. K. A. Stetson and R. L. Powell, "Interferometric hologram evaluation and real-time vibration analysis of diffuse objects," *J. Opt. Soc. Am.* **55**, 1694–1695 (1965).
7. G. Pedrini, W. Osten, and M. E. Gusev, "High-speed digital holographic interferometry for vibration measurement," *Appl. Opt.* **45**, 3456–3462 (2006).
8. M. Hytch et al., "Nanoscale holographic interferometry for strain measurements in electronic devices," *Nature* **453**, 1086–1089 (2008).
9. H. M. Shang et al., "Surface profiling using shearography," *Opt. Eng.* **39**, 23–31 (2000).
10. H. Lee, A. J. Rosakis, and L. B. Freund, "Full-field optical measurement of curvatures in ultra-thin-film-substrate systems in the range of geometrically nonlinear deformations," *J. Appl. Phys.* **89**, 6116–6129 (2001).
11. H. V. Tippur, "Simultaneous and real-time measurement of slpoe and curvature fringes in thin structures using shearing interferometry," *Opt. Eng.* **43**, 3014–3020 (2004).
12. T. C. Chu et al., "Application of digital-image-correlation techniques to experimental mechanics," *Exp. Mech.* **25**(3), 232–244 (1985).
13. B. Pan et al., "Two-dimensional digital image correlation for in-plane displacement and strain measurement: a review," *Meas. Sci. Technol.* **20**, 062001 (2009).
14. B. Pan et al., "High-temperature digital image correlation method for full-field deformation measurement at 1200°C," *Meas. Sci. Technol.* **22**, 015701 (2011).
15. M. Pankow, B. Justusson, and A. M. Waas, "Three-dimensional digital image correlation technique using single high-speed camera for measuring large out-of-plane displacements at high framing rates," *Appl. Opt.* **49**, 3418–27 (2010).
16. C. Periasamy and H. V. Tippur, "Full-field digital gradient sensing method for evaluating stress gradients in transparent solids," *Appl. Opt.* **51**(12), 2088–2097 (2012).
17. C. Periasamy and H. V. Tippur, "A full-field reflection-mode digital gradient sensing method for measuring orthogonal slopes and curvatures of thin structures," *Meas. Sci. Technol.* **24**, 025202 (2013).
18. W. Hao et al., "Experimental study on the fiber pull-out of composites using digital gradient sensing technique," *Polym. Test.* **41**, 239–244 (2015).
19. C. Zhang et al., "Full-field measurement of surface topographies and thin film stresses at elevated temperatures by digital gradient sensing method," *Appl. Opt.* **54**, 721–727 (2015).
20. A. S. Jain and H. V. Tippur, "Extension of reflection-mode digital gradient sensing method for visualizing and quantifying transient deformations and damage in solids," *Opt. Lasers. Eng.* **77**, 162–174 (2016).

21. X. Dai et al., "Thermal residual stress evaluation based on phase-shift lateral shearing interferometry," *Opt. Lasers Eng.* **105**, 182–187 (2018).
22. C. Miao et al., "Surface profile and stress field evaluation using digital gradient sensing method," *Meas. Sci. Technol.* **27**, 095203 (2016).
23. C. Miao and H. V. Tippur, "Measurement of sub-micron deformations and stresses at microsecond intervals in laterally impacted composite plates using digital gradient sensing," *J. Dyn. Behav. Mater.* **4**(3), 336–358 (2018).
24. C. Miao and H. V. Tippur, "Fracture behavior of carbon fiber reinforced polymer composites: an optical study of loading rate effects," *Eng. Fract. Mech.* **207**, 203–221 (2019).
25. C. Miao and H. V. Tippur, "Higher sensitivity digital gradient sensing configurations for quantitative visualization of stress gradients in transparent solids," *Opt. Lasers Eng.* **108**, 54–67 (2018).
26. L. Huang et al., "Comparison of two-dimensional integration methods for shape reconstruction from gradient data," *Opt. Lasers Eng.* **64**, 1–11 (2015).

Chengyun Miao obtained BS degree from Soochow University, China in 2013. Currently, he is a PhD candidate in mechanical engineering at Auburn University. His interests include developing optical techniques and applying them to study dynamic failure behavior of engineering materials. He has developed a full-field optical metrology tool to measure surface topography of thin films at submicron accuracy over large areas, and two novel enhanced sensitivity optical sensors for metrology of transparent ceramics. He has applied different optical techniques to study fracture mechanics of fiber reinforced polymer composites, glass and cellulose nanopapers. His coauthored publications include five archival journals and three conference publications. He has received the Outstanding Reviewer Award from IOP Publishing, and named Outstanding International Graduate Student by Auburn University.

Hareesh V. Tippur is the McWane Endowed Chair professor of mechanical engineering at Auburn University, Alabama. He has worked extensively in the areas of fracture and failure mechanics with an emphasis on high-strain rate material behavior. He is credited with the development or advancement of quantitative visualization tools including speckle and moiré methods, coherent gradient sensing, infrared interferometry, digital image correlation, and digital gradient sensing. His works have examined failure mechanics of dissimilar material interfaces, functionally graded materials, syntactic foams, interpenetrating phase composites, and nanocomposites. To date his works have resulted in over 200 publications in journals, books and conference proceedings. He has received accolades from national and international societies including SEM, ASEE, ASME, BSSM, and ICCES. He was the editor-in-chief of *Experimental Mechanics* and currently serves on the editorial committees of *Strain*, *Journal of Dynamic Behavior of Materials*, and *Journal of Engineering Materials and Technology*.